

First results from the UCSC Laboratory for Adaptive Optics multi-conjugate and multi-object adaptive optics testbed

S. Mark Ammons^a, Renate Kupke^a, Edward A. Laag^{a, b}, Donald T. Gavel^a, Daren R. Dillon^a, Marco R. Reinig^a, Brian J. Bauman^{c, a}, Claire E. Max^a, Jess. A. Johnson^a

^aCenter for Adaptive Optics, University of California, Santa Cruz, 1156 High St., Santa Cruz, CA 95064, USA;

^bUniversity of California, Riverside, 900 University Avenue, Riverside, CA, 92521, USA;

^cLawrence Livermore National Laboratory, 7000 East Avenue, Livermore, CA, 94550, USA

ABSTRACT

We present first results from the Multi-Conjugate and Multi-Object Adaptive Optics (MCAO and MOAO) testbed, at the UCO/Lick Laboratory for Adaptive Optics (LAO) facility at U.C. Santa Cruz. This testbed is constructed to simulate a 30-m telescope executing MCAO and/or open loop MOAO atmospheric compensation and imaging over 5 arcminutes. It is capable of performing Shack-Hartmann wavefront sensing on up to 8 natural or laser guide stars and 2-3 additional tip/tilt stars. In this paper, we demonstrate improved on-axis correction relative to ground layer adaptive optics ($\sim 15\%$ Strehl relative to $\sim 12\%$) with a simulated 28-m aperture at a D/r_0 corresponding to a science wavelength of 2.6 microns using three laser guide stars on a simulated 41 arcsec radius with a central science object and one deformable mirror at the ground layer.

Keywords: multi-conjugate, multi-object, adaptive optics, deformable mirror

1. INTRODUCTION

Traditional single-conjugate adaptive optics (SCAO) has carved new paths for astronomical studies on large telescopes, providing diffraction-limited imaging for the narrow field at moderate sky coverage. However, the desire for wide-field resolved imaging from the ground has spurred thought on multi-conjugate adaptive optics (MCAO), the technique of using several deformable mirrors at varying conjugate heights to correct for a much larger volume of atmospheric turbulence. Such a correction requires sensing turbulence with many guide stars spread throughout the science field. Also being considered for both existing and future large telescopes is multi-object adaptive optics (MOAO), a technique of applying single conjugate correction in several different directions and leaving the rest of the field uncorrected. Both approaches require multiple deformable mirrors and multiple laser guide stars to enable good sky coverage. An alternate direction being considered for large telescopes is to vastly improve Strehl for narrow-field SCAO by tackling the cone effect with several laser guide stars. All three scenarios necessitate optimal wavefront estimation using information from multiple laser guide stars, however high-Strehl narrow-field SCAO and MOAO differ from MCAO in requiring only a single deformable mirror.

MCAO is currently being demonstrated on testbeds throughout the world, like the MAD demonstrator,¹ a facility class MCAO instrument intending to achieve correction over 2 arcminutes in the K band for the Very Large Telescope (VLT). The 8-m Gemini South telescope has similar requirements for a laser guided MCAO system with first light in 2007.² MCAO experiments have already been completed on solar telescopes, most notably the Dunn Solar Telescope,³ using cross-correlation centroiding techniques for wavefront sensing. MCAO was first demonstrated in the lab by Per Knutson in 2004 with two low-order deformable mirrors in a simulation of a 7.5 meter telescope.⁴

Further author information: (Send correspondence to S.M.A.)

S.M.A.: E-mail: ammons@ucolick.org, Telephone: 1 831 459 1637

D.T.G.: E-mail: gavel@ucolick.org, Telephone: 1 831 459 5464

Facility instruments for world-class telescopes must incorporate detailed laboratory investigation, starting many years before their planned operation. As with all large engineering ventures, the testbed phase becomes more significant as the cost and scale of the instrument increases. The MCAO/MOAO testbed at the Laboratory for Adaptive Optics at UCSC was constructed to answer critical questions about future wide field adaptive optics systems on large telescopes. It is designed to be modular, with interchangeable components that enable switching between MCAO, MOAO, and narrow-field high-Strehl systems in a minimal amount of time. The initial testbed is complete and ready for reconfiguration that enables testing full MCAO operation with 3 deformable mirrors and 8 laser guide stars, as well as multi-iteration open loop capabilities for MOAO tests.

In this paper we describe the testbed as well as present our initial experiment to demonstrate the system operations. Our first experiment is a single iteration, open-loop correction of a central science star using a circular constellation of 3 laser guide stars with 1.4 arcmin diameter. Improved Strehls are obtained relative to GLAO ($\sim 15\%$ and $\sim 12\%$, respectively) for a 28-m telescope with a 3-layer atmospheric profile that simulates a D/r_0 corresponding to a science wavelength of 2.6 microns. GLAO is here referred to as an averaging of wavefronts before application to a single deformable mirror. Section 2 presents the design and optical layout of the testbed. We summarize the basic control and software designs in Section 3 and outline methods of alignment and calibration in Section 4. In Section 5, we describe preliminary open-loop tomography results. We discuss our initial estimate of systematic errors in Section 6.

2. TESTBED LAYOUT

The MCAO/MOAO testbed at the Laboratory for Adaptive Optics at UCSC is currently testing crucial concepts for MCAO, MOAO, and narrow-field high-Strehl adaptive optics. The complete design of the testbed, cursorily introduced here, will be presented in detail in a future publication. The testbed simulates a thirty meter telescope with up to six atmospheric layers and three deformable mirrors. The MCAO testbed utilizes three Hamamatsu X8267-16 Programmable Phase Modulators (PPMs) as deformable mirrors, with 768x768 pixels. Three Shack-Hartmann wavefront sensors are used with 64 subapertures across the 30 meter pupil, upgradable to 9 guide stars with 100x100 sampling by multiplexing sensors on our Dalsa 1024x1024 cameras. The laser guide stars are simulated with pigtail fibers embedded in an aluminum plate that has been machined to include several predetermined constellation configurations. A science laser, split from the same 658 nm Crysta double YAG diode laser as the laser guide stars, is coupled into the system via a 75 mm plate beamsplitter.

The testbed layout is shown in Fig. 1. Several slots are available for different types of deformable mirrors, which may be conjugated to different atmospheric heights. The PPM devices consist optically addressed spatial light modulators (SLM) with 20x20 mm apertures. These SLMs are optically coupled to liquid crystal displays (LCDs) upon which desired phase patterns can be displayed. The optical coupling between the LCD and SLM blurs pixelation, decreasing the diffractive effects seen in typical liquid crystal devices. For practical purposes, the device functions as a VGA monitor, allowing the phase map to be sent as a simple graphics image displayed on 768x768 separately addressed pixels. Also, the PPMs operate on linearly polarized light, with the direction of polarization determining whether the PPMs modulate phase, intensity, or some combination of both. The PPMs have a limited stroke of 7.8 radians at the center of the array and 6.2 radians near the edges, requiring that P-V excursions exceeding these limits be phase wrapped. Phase wrapping with PPMs has proven to be robust in vision science applications,⁵ in which adaptive optics systems are used to correct quasi-static aberrations in the human eye. See Section 6.2 for details regarding the interactions between phase wrapping and the Hartmann sensors and the resulting wavefront error.

We use a linear polarizer after the telescope primary, which serves the double purpose of (1) polarizing the light for the PPM and (2) permitting the intensity of any of the laser guide or science stars to be individually tuned by changing the input polarization of the diodes.

We simulate an atmosphere with six etched phase plates manufactured by Lawrence Livermore National Laboratory's microfabrication facility. A phase screen pattern with a Kolmogorov power dependency was generated and used for each plate. The plates have different etch depths for each pattern to produce different Fried's parameters r_0 and simulate varying turbulence strengths for atmospheric layers. The step-etching was performed with hydrofluoric acid to change the optical path length, creating an achromatic turbulence profile.

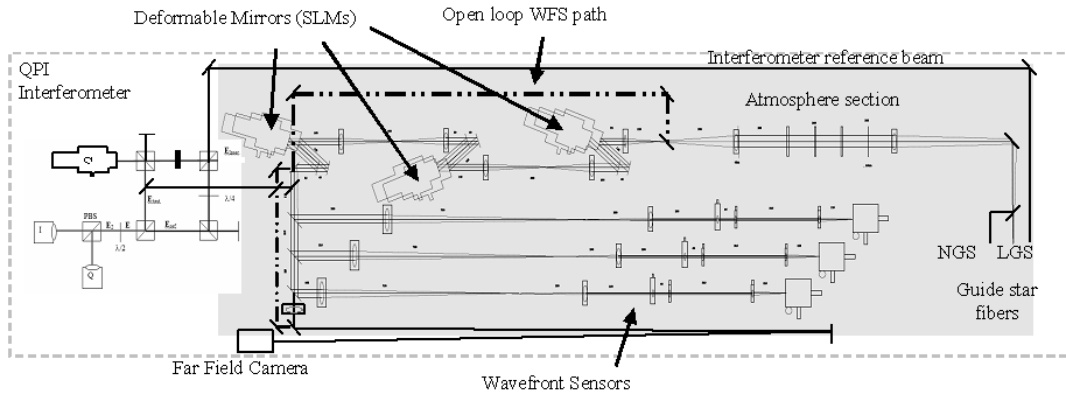
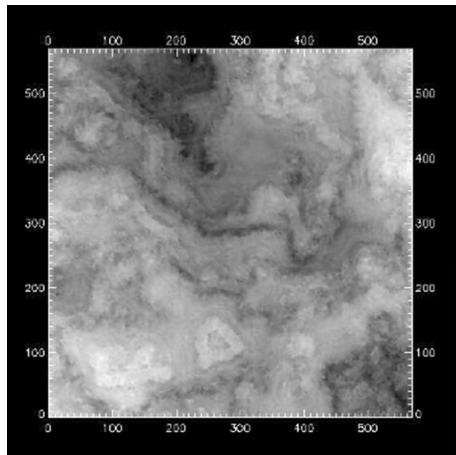


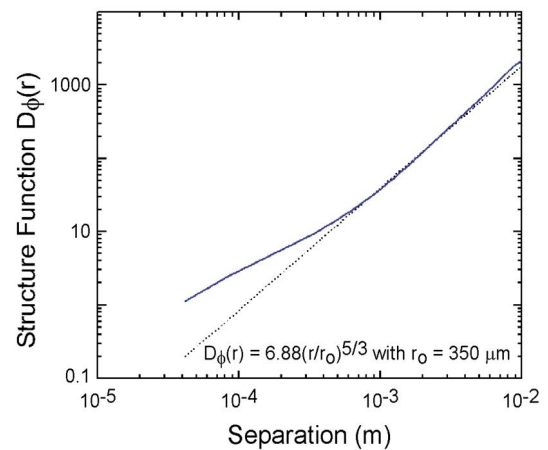
Figure 4. Multi-guidestar next generation AO testbed layout showing MCAO and MOAO configurations

Figure 1. Optical layout for MCAO/MOAO testbed, in MCAO form.

8 etched steps are used to simulate 8-bits of dynamic range. The lowest bit depth is 25 nm, contributing to error beyond the control frequencies (see Section 6.4). The plates are motorized in the atmosphere section of the MCAO/MOAO bench, and may be moved with preselected speeds to replicate observed wind velocities and simulate a dynamic atmosphere. Key parameters for the atmospheric plates are given in Table 1, including plate r_0 and fitting error. A phase image of a single plate, measured with an interferometer, is given in figure 2. Also shown is the measured structure function and the fitted Kolmogorov power spectrum.



(a)



(b)

Figure 2. (a) Interferometer phase image of a Kolmogorov phase screen. Notice the persistent circular patterns caused by the etching. (b) Structure function for the accompanying phase screen, with a fitted Kolmogorov spectrum. Notice the tail at uncontrollably high spatial frequencies.

Our three Shack-Hartmann sensors utilize AoA square-pack lenslet arrays with 100 micron pitch and 1.7 mm focal length. With this spacing, we are able to sample the wavefront with 64 16x16 pixel subapertures across each of three Dalsa CCDs. This size is necessary to (1) simulate guide star elongation for a thirty meter telescope, (2) improve the linearity of wavefront sensors to enable open loop operation, (3) permit large wavefront excursions (including wrapping) without aliasing into neighboring subapertures, and give freedom of choice of centroiding methods without read noise or photon noise restrictions. The wavefronts sensors utilize spatial filters to further

Table 1. Table of critical parameters for etched atmospheric plates. The column of Piston/Tip-Tilt removed RMS errors are the mean errors for all pupils of 26.6 mm in size, or a 28 meter telescope, with 52 subapertures across the diameter. r_0 is calculated at the bench wavelength of 658 nm. The final column lists Strehls obtained for open-loop SCAO on these individual plates at 0 km altitude. Strehls are calculated as described in the footnote at the end of this section.

Screen #	P-V OPD (μm)	r_0 (mm)	Pist/TT removed RMS (nm)	Fitting error (nm)	Mean Strehl
1	14.4	0.700	660	42.5	40%
2	5.00	2.489	229	14.8	65%
3	6.16	1.931	283	18.2	56%
4	3.34	4.023	154	9.9	75%
5	2.82	4.926	130	8.4	82%
2+4+5	-	1.767	305	20.0	41%

prevent aliasing errors (see Poyneer and Macintosh 2003⁶), which for these purposes are circular irises at the focal plane ahead of each lenslet array. We are currently upgrading to 8 laser guidestars by optically multiplexing 4 guide stars on each Dalsa camera and halving the subaperture size. The static errors on the laser guide stars, after removal of tip/tilt and focus, range between 0.8 and 1.5 microns RMS across the thirty meter pupil and are principally composed of off-axis coma and astigmatism. The laser guide stars are off-axis through the entire optical system upstream of the wavefront sensors. They are on-axis in the sensors, which are individually aligned to single guide stars.

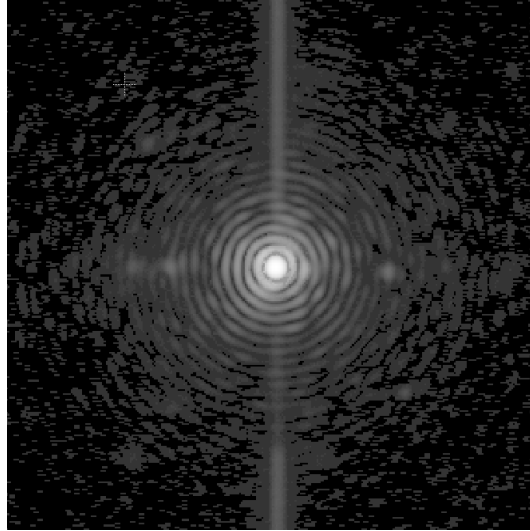
The science camera is a Point Grey Flea 1024x768 CCD at the focus of an F-43 beam. This camera observes the on-axis science star at the center of the laser guide star constellation. Because Strehl measurement is not the most direct method of wavefront quality, we are currently adding a leg to the MCAO/MOAO bench to directly feed the Quadrature Polarization Interferometer (QPI), intending to use it as a truth interferometer. The QPI is described in Section 4.2.

The on-axis static error through the entire system on the science star, tip/tilt and focus removed, is 60 nm RMS of astigmatism due to optical misalignment without atmospheric plates. This error is partially corrected by a PPM to give a static Strehl of 97%.* The static corrected point spread function (PSF) is shown in Figure 3; it's radial profile is compared to a theoretical diffraction-limited PSF in Figure 8. Ghost image flux has been subtracted in the Strehl calculation above.

3. SOFTWARE AND CONTROL

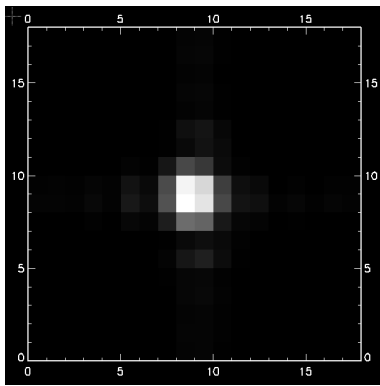
We are currently using a cross-correlation centroider with a Gaussian reference with a width determined empirically, as exemplified in Poyneer et al. 2005.⁷ Our Hartmann subapertures have very little read noise and photon noise, but the sinc functions possess a great deal of structure that depends on the wavefront features within that subaperture (several subapertures are shown in Fig. 4). For example, the atmospheric plates possess high-frequency contours that reduce the overall intensity in individual subapertures and cause asymmetries in the principal spot. Phase wraps in the PPM's are high-frequency features that are blocked by the wavefront sensor spatial filters and cause intensity loss as well. In addition, in the presence of large atmospheric wavefront error, these features and other sinc function nodes may cross over into neighboring subapertures. Gaussian cross-correlation has been shown to be robust under these circumstances,⁸ although center of mass with windowing demonstrates similar results with less computation time. Our experiments with non-windowed, thresholding center of mass routinely give poorer Strehl than Gaussian cross-correlation.

*Strehl is here calculated as the ratio of the max value in DN to the total power over a radius of 40 Airy rings relative to the same ratio for a computer-generated diffraction-limited Airy pattern at the same pixel sampling. This ratio, averaged over all possible sub-pixel offsets to eliminate sampling error, is 0.0235 for our plate scale.

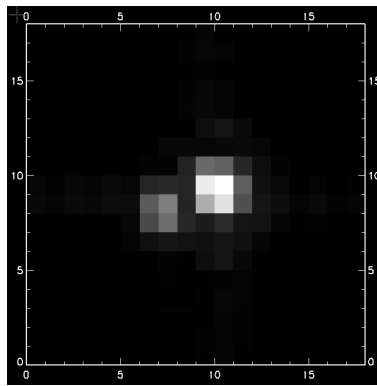


(a)

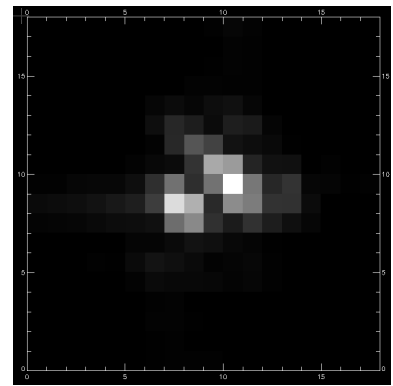
Figure 3. Point spread function for static correction with no atmosphere, log stretch to the 0.25 power.



(a) Subaperture with no atmospheric wavefront error.



(b) Subaperture with 450 nm RMS atmospheric wavefront error over a 30-m pupil.



(c) Subaperture with 1500 nm RMS atmospheric wavefront error over a 30-m pupil.

Figure 4. Typical image of individual subapertures for several cases of atmospheric wavefront error. Notice the amplitude growth of non-Gaussian structure as the wavefront aberration increases.

Slopes are explicitly reconstructed into wavefronts with Fourier techniques.⁹ The wavefronts from all sensors undergo processing, which includes depistonning, edge treatment, dewarping (see Section 4), and possibly tomographic analysis if desired for MCAO/MOAO. In open loop operation, the final wavefronts are applied to the PPMs with a variable gain that depends on the amount of atmospheric wavefront error being corrected.

3.1. Architecture

The control software for the testbed is written in Interactive Data Language (IDL) in an object-oriented style, in which each main program has command over the testbed and calls a number of support routines to accomplish specific tasks. The advantage to this style has been that each routine can be thoroughly tested before implementation and commonly used blocks of code are the same for every main program. An example program for doing tomography in an MOAO configuration with 1 DM at the 0km conjugate pupil is shown in block form in

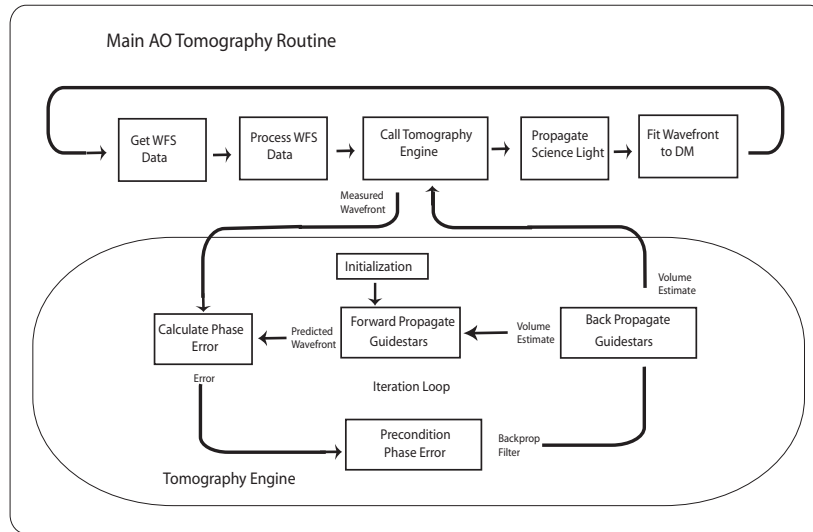


Figure 5. Simplified block diagram of closed loop iterations, with tomographic iterations illustrated. In the single-iteration open loop tomography experiment discussed in Section 5, the loop is broken after fitting the wavefront to the PPM.

figure 5. This configuration may be expanded for use with multiple DMs.

The tomography engine is “Tomography Spherical Wave” by Don Gavel for simulation purposes, modified to support tomography on the testbed. The bulk of the computation occurs in a *for* loop during which we build up an estimate of the δ optical path differences (OPDs) at each layer through a series of forward and back propagations of guidestars. The computationally intensive calculations are performed in Fourier space, so there are filtering steps to prevent “ringing” from Fourier transforms. The method is conceptually described in Gavel 2004.

When the tomography engine is called it first initializes itself based on a number of user selectable parameters, including physical values for the atmosphere and various switches. The user chooses the atmosphere to be simulated, the guidestar configuration, and number of science objects. The atmosphere is then created. This step determines the number of turbulent layers, their respective heights, r_0 , the C_n^2 profile, and determines the size of the volume estimate array. When this is completed, the back propagation filter is created.

The main loop begins with a forward propagation step through the volume estimate, producing a predicted wavefront. This predicted wavefront is then subtracted from the measured wavefront to calculate phase error. This phase error is then preconditioned using the back propagation filter (equation 16 in Gavel 2004). In the back propagation step, phase errors are coadded to the respective layers in the volume estimate to produce a revised volume estimate. The guidestar light is then forward propagated through the volume estimate and the process is iterated until the phase error reaches a tolerance set to roughly the level of the measurement error.¹⁰

4. ALIGNMENT AND CALIBRATION

4.1. Field distortion

The large number of reimaged pupil planes and focal planes in MCAO systems, each with different optical components that create their own share of field-dependent wavefront error and field distortion, complicate attempts at registering wavefront sensors to deformable mirrors. Our current master reference plane is a physical pupil located at the image of the ground layer that sets the telescope diameter. It is between the wavefront sensor section and the deformable mirror section. It is possible to place intensity modulations (gratings) exactly at this plane to which the wavefronts sensors may be individually registered. Then, phase modulation may be applied to individual deformable mirrors to generate distortion maps for each wavefront sensor. Intensity modulations

may also be applied at the true ground layer (which has no overlaying optics) to register wavefront sensors to this plane.

In the current configuration, with one deformable mirror and three sensors, phase modulation is applied to the PPM in the form of 20 Gaussian bumps with widths of one Hartmann subaperture. However, the error of the measured centroid of the Gaussian phase bump depends heavily on the exact location of the Gaussian within a subaperture. We therefore use a scheme in which the bumps are driven in closed loop to the centers of Hartmann subapertures so that all Gaussian bumps experience the same sampling error bias. The positions of the Gaussians are used to generate a warping map for each wavefront sensor, which may be applied in reverse to dewarp wavefronts with the IDL “tri_warp” function. This technique will not be available for conventional types of deformable mirrors or MEMS devices, as thin Gaussian bumps cannot be shifted by fractions of a subaperture on these mirrors.

The second and higher order components of the warping between Hartmann sensors and the ground layer PPM is small, with P-V deviations of 2 PPM pixels, or 10% of a Hartmann subaperture. The rotation component is large, on the order of several degrees, due to the optical tilt of the PPM and the change of height of several downstream components.

4.2. Generating a PPM lookup table

The PPM devices were calibrated using the Quadrature Polarization Interferometer (QPI) at the Laboratory for Adaptive Optics. This modified Mach-Zehnder interferometer contains a quarter-wave plate on the reference leg, converting the laser’s linearly-polarized light to circularly-polarized light. The test leg polarization is rotated 45 degrees by a half-wave plate. After the test and reference legs recombine, the polarizations are separated by a polarizing beamsplitter cube, and both are imaged simultaneously onto two CCD cameras. This configuration allows measurement of both the cosine (real) and sine (imaginary) parts of the wavefront phase simultaneously. These, coupled with the intensity amplitude (obtained by incoherently summing images taken with the reference and test arms blocked), provide enough information to unambiguously reconstruct the wavefront.

The PPMs are addressable over 8-bits of intensity, corresponding to an approximate 2π phase change on the reflected beam. To measure this precisely, the PPM was placed on the test arm of the QPI. A number of rows (336) on the left side of the device were held at a data number of 128, while the remaining rows on the right side of the device were stepped from 0 to 255 in increments of 4. At each data number, an interferometric data set consisting of the two complimentary fringe images, as well as a signal and reference arm image for each camera, were taken, and a phase map was obtained. This procedure was repeated, holding the right 336 rows at 128, while ramping the left portion of the device from 0-255. In this way, a response curve for each pixel of the device was acquired.

The response curves are smoothed and inverted to generate a lookup table. Plots of these inverted response curves, as well as the PPMs “flat” phase, are given in Fig. 6. Notice that the “flat” phase generated by the PPM has a natural cylinder shape (astigmatism plus focus).

5. PRELIMINARY OPEN LOOP TOMOGRAPHY EXPERIMENT

Atmospheric Tomographic Reconstruction is a method of wavefront estimation in which a three-dimensional distribution of index of refraction variation is generated as an intermediate step. Many future adaptive optics system designs that utilize multiple laser guide stars, including MCAO/MOAO and high-strehl systems, may use a variant of tomographic reconstruction methods to perform optimal estimation and open loop correction. It is crucial to understand and test these algorithms with testbed installations, so as to make choices educated by the acquisition of real performance data.

We here demonstrate the utility of the LAO MCAO/MOAO bench by investigating the tomography algorithm of Gavel 2004¹¹ under open loop operation. The experimental setup is as described in section 2, with only one PPM being utilized to correct in a single direction. Three laser guidestars are arranged in a circle of radius 1.4 arcminutes, with a central science star. Only one iteration is performed on a static atmosphere to obtain an instantaneous open-loop Strehl. For the magnitude of wavefront errors considered here, the wrapping error addressed in Section 6.2 prevents the Hartmann sensors from reading the resulting wavefront residuals effectively,



(a) Plots of PPM response curves, 8-bit PPM commands vs. real phase in nm, for several PPM pixels.

(b) Flat shape of PPM, corresponding to 8-bit PPM commands that flatten the device.

(c) Wrapped wavefront, applied to PPM in the open loop tomography experiment on a 550 nm P-V error.

Figure 6.

so we are currently limited to single iterations. The atmosphere is distributed as follows: Plate 2 ($r_0 \sim 2.489$ mm) at 0 km, Plate 4 ($r_0 \sim 4.023$ mm) at 5.95 km, and Plate 5 ($r_0 \sim 4.926$ mm) at 13.3 km. The D/r_0 that corresponds to this case may be obtained from the measured wavefront error by¹²

$$\sigma_N^2 = 0.134(D/r_0)^{(5/3)}$$

when the tip/tilt error is subtracted. This equation gives $D/r_0 = 21.7$ for the mean measured error of 500 nm for the atmospheric plate configuration described above. With a simulated 28-m aperture, this corresponds to an r_0 of $28 \text{ m} / 21.7 = 1.29 \text{ m}$ or a simulated science wavelength of 2.6 microns, assuming that $r_0 = 18 \text{ cm}$ at an extremely good site.

The preliminary open loop Strehls obtained are recorded in Table 2. The first row describes Strehls taken when the turbulence plates (2, 4, and 5) are collected at the ground layer and single-conjugate AO is used. This SCAO Strehl represents the base error present in all further data and is the maximum Strehl attainable. The next three rows describe Strehls for different realizations of a true 3-layer atmosphere, but with turbulence heights staying constant at 0, 5.95, and 13.3 km altitudes. The final row represents the mean of the Strehls for the three realizations. Strehls are given for four cases: (1) Tomography, in which the tomographic algorithm of Gavel 2004 is used to estimate an optimal wavefront in the science direction; (2) GLAO, in which the wavefronts from all three sensors are simply averaged and placed on the single PPM; (3) SCAO, in which only one of the guide star wavefronts is applied to the PPM; and (4) no adaptive optics correction is applied. All Strehls are instantaneous Strehls, using the location of the maximum value of the image as the diffraction-limited core. The instantaneous Strehl is an overprediction of the time-averaged performance for images with Strehls less than 10%, at which point the image is generally not diffraction-limited and the time-averaged maximum value is typically much less.

The point spread functions (PSFs) are shown in figure 7. Both the intensity maps and profiles are log-stretched to bring out detail in the wings. PSFs are shown for all four cases enumerated above, averaged over the three atmospheric realizations given in the table, as well as the single-conjugate case with all turbulence layers at the ground. The radial profiles are compared for these five cases, along with the static corrected PSF with no atmosphere and a theoretical Airy function.

6. CURRENT SYSTEM LIMITATIONS

As the experiments above are strictly exploratory and the results are precursors to further improvements, we do not build a rigorous error budget in this forum. In this section, we suggest errors that may contribute to Strehl degradation for this experiment.

Table 2. Preliminary results from the open loop tomography experiment. The percent Strehls are calculated as ratios of the max value in DN to the total power over a radius of 40 Airy rings relative to the same ratio for a computer-generated diffraction-limited Airy pattern at the same pixel sampling.

Atmosphere case	Mean RMS (nm)	Tomography Strehl	GLAO Strehl	SCAO Strehl	no AO Strehl
Plates at ground	415	-	-	41.9%	1.9%
Realization 1	425	19.4%	12.9%	4.1%	2.0%
Realization 2	498	13.6%	13.6%	6.6%	1.4%
Realization 3	550	11.0%	9.0%	3.0%	1.6%
Mean	491	14.7%	11.8%	4.6%	1.7%

6.1. Wavefront sensor disagreement

With tip/tilt and piston errors removed, the wavefront sensors agree to 2-3 nm RMS over a 30-m pupil when differenced, implying that the air on the bench and the wander of optics is negligible. However, if tip/tilt is not removed, the wavefront sensors tend to disagree by 20-30 nm RMS, or 60-90 nm P-V. There appears to be a noncommon tip/tilt wander present in the individual wavefront sensors with magnitude 20 nm. There is also a tip/tilt wander common to all three sensors due to movement of upstream optics, with a magnitude of 20 nm RMS. Other statistics of the wavefront sensor agreement are shown in Table 3. Note that the presence of wavefront error greatly increases the disagreement, suggesting that wavefront sensor nonlinearity is a major source of error.

Table 3. Mean RMS measurements, in nanometers, of wavefront sensor disagreement for one minute after taking references. 10 coadds of Hartmann frames are taken over a short time span. The three wavefront sensors were differenced in pairs and the three combinations of differences were averaged to obtain the numbers. In the experiments in the second column, piston and tip/tilt are determined and subtracted for each individual wavefront sensor. For the third column, individual piston and mean tip/tilt are subtracted. In the final column, only individual piston is subtracted. Five bench conditions are given, including several cases with no atmosphere to illustrate the benefits afforded by baffling. The wavefront sensor disagreement increases linearly with the strength of the wavefront error introduced.

Conditions	Piston/TT removed	Piston/Common TT removed	Piston removed
no atmos, no baffling	24	54	59
no atmos, baffling	4.1	14	23
Plate 2, 350 nm RMS	52	128	144
Plate 1, 850 nm RMS	91	139	170

6.2. Wrapping Error

As mentioned in Section 2, the PPM devices must wrap phase to achieve the P-V deviations required by a normal atmosphere. An example of the wrapped phase for the atmosphere cases in section 5 is shown in figure 6. These deviations do not largely affect the PSF formation. When the PPM is set to its nominal “flat” shape, only the static error of the bench is left remaining (with $\sim 60\%$ Strehl). If single-wave stripes are added to the PPM commands, so that the device is forced to wrap phase for each stripe, the Strehl is degraded by only a few points to $\sim 57\%$, indicating that 20-30 nm of error is attributable to phase wrapping.

However, Hartmann sensors are not immune to phase wraps. The phase wraps are not perfect phase jumps, possessing a smooth transition area from 0 to 2π phase. The width of this transition area is 4 PPM pixels or one-third of a Hartmann subaperture. Phase wraps that occur on subaperture boundaries tend to bias the

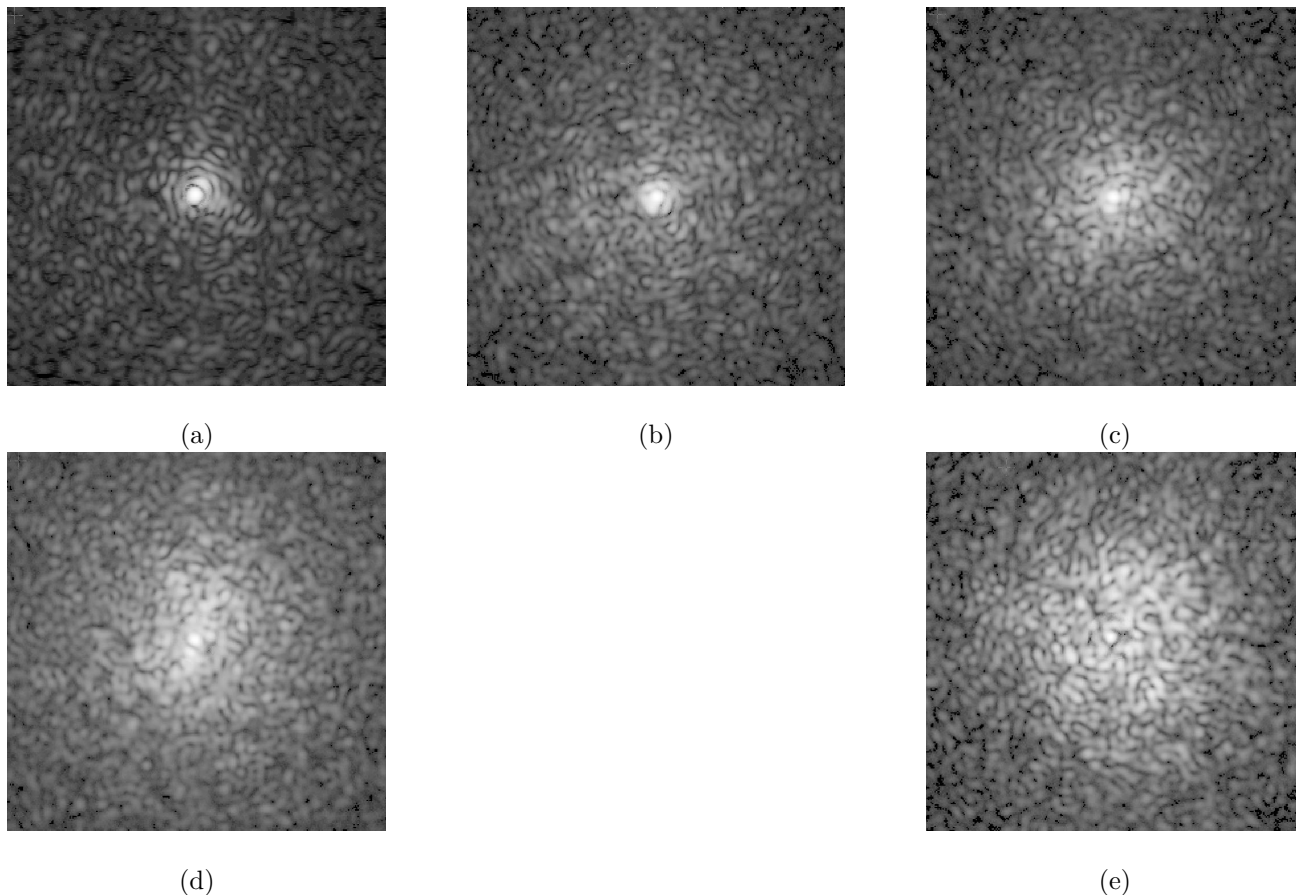


Figure 7. On-axis point spread functions for the science star are shown with a logarithmic + 0.25 power stretch for the preliminary open loop tomography experiment. The PSFs have been obtained with three different exposures using ND filters to bring out the details in the PSF wings. (a) Single conjugate case with all plates at the ground. (b) Case with tomographic wavefront estimation. (c) Ground layer adaptive optics (GLAO) case - all wavefronts are averaged. (d) Single conjugate AO (SCAO) case - single wavefront applied to PPM. (e) No adaptive optics correction.

centroid on both sides by between 0.3 and 1.0 pixels. We have written procedures to mask out such phase errors, but these become unreliable when the number of phase jumps across the pupil is large (on the order of 5-10). Therefore, closed loop operation becomes difficult for large phase excursions, and the minimum closed loop error achieved is typically some fraction of the total RMS error being corrected. In addition, the closed-loop stability time is much shorter for larger errors. We are investigating further solutions to this error, but in the current paper we avoid the issue altogether by operating open-loop and taking wavefront sensor measurements only when the PPM is not wrapping phase.

6.3. PPM scattering

The PPMs have structure at extremely high frequencies due to their small-scale pixelation. This frequency is ~ 12 times the subaperture spacing frequency, which is undetectable, but which manifests itself as a set of grid-like diffraction orders surrounding the laser guide stars. This causes an intensity loss in the stars themselves, but the PSF is not disturbed in the control band, so the Strehl is largely unchanged. However, because we use multiple laser guide stars, the diffraction spikes from one star may fall very near other guide stars, disturbing the wavefront sensor measurement. We currently address this with spatial filters, which are effective at removing this contamination. Future upgrades to 8 or 12 guide star will necessitate rotation of the PPM to isolate all diffractive orders from real guide stars.

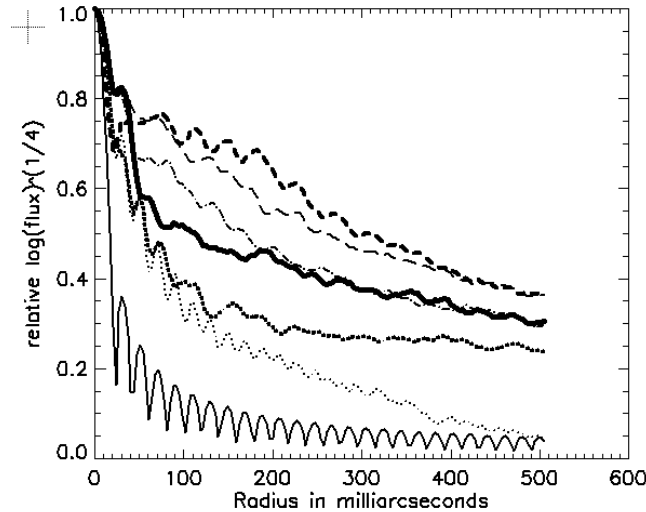


Figure 8. Comparison of radial profiles. Fluxes are converted to logarithmic space and then exponentiated to the 0.25 power to bring out low-intensity details. The lower solid line is a theoretical Airy function for our plate scale. The thin dotted line is the static PSF with no atmosphere. The thick dotted line is the case in which all atmospheric plates have been moved to the ground to obtain an upper limit on the system Strehl. The thick solid line represents the performance of the tomography engine. The dashed-dotted line is the profile for GLAO, or wavefront averaging. The thin dashed line is the performance with SCAO, or when only one single off-axis wavefront sensor is used. Finally, the thick dashed line is the radial profile when no adaptive optics is being used. Notice that the principal advantage of tomography over GLAO is apparent in the mid-to-low frequency range.

6.4. Atmospheric Plate scattering

The turbulence plates we use to simulate the atmosphere possess extra high-frequency information due to the discrete step-like nature of the bit-etching. Notice in figure 2 that the structure function of the plates (identical for all plates, but scaled horizontally for different plates) has a long tail beyond the Kolmogorov spectrum at high frequencies. This high frequency information is random and has no favored direction, so it is unlikely that it would alias into low frequency errors in the wavefront sensors. Nevertheless, the spatial filters we employ at each wavefront sensor are effective at blocking this high-frequency content. The RMS error from this contribution is roughly 8 nm for the smallest plate and up to 20 for the largest (plate 1).

ACKNOWLEDGMENTS

The authors are grateful for funding from the Moore foundation, whose generous gift enabled the construction of the Laboratory for Adaptive Optics at the University of CA, Santa Cruz. The authors also acknowledge the NSF for the Science and Technology Centers grant to fund the Center for Adaptive Optics as well as the GRFP (SMA).

REFERENCES

1. E. Marchetti, N. N. Hubin, E. Fedrigo, J. Brynnel, B. Delabre, R. Donaldson, F. Franza, R. Conan, M. Le Louarn, C. Cavadore, A. Balestra, D. Baade, J.-L. Lizon, R. Gilmozzi, G. J. Monnet, R. Ragazzoni, C. Arcidiacono, A. Baruffolo, E. Diolaiti, J. Farinato, E. Vernet-Viard, D. J. Butler, S. Hippler, and A. Amorin, "Mad the eso multi-conjugate adaptive optics demonstrator," *proc. SPIE* **4839**, p. 317, 2003.
2. B. L. Ellerbroek, F. J. Rigaut, B. J. Bauman, C. Boyer, S. L. Browne, R. A. Buchroeder, J. W. Catone, P. Clark, C. d'Orgeville, D. T. Gavel, G. Herriot, M. R. Hunten, E. James, E. J. Kibblewhite, I. T. McKinnie, J. T. Murray, D. Rabaud, L. K. Saddlemyer, J. Sebag, J. Stillburn, J. M. Telle, and J.-P. Veran, "Multiconjugate adaptive optics for gemini-south," *proc. SPIE* **4839**, p. 55, 2003.

3. M. Langlois, G. Moretto, K. Richards, S. Hegwer, and T. R. Rimmele, "Solar multiconjugate adaptive optics at the dunn solar telescope: preliminary results," *proc. SPIE* **5490**, p. 59, 2004.
4. P. A. Knutsson and M. Owner-Petersen, "The lund dual-conjugate adaptive optics demonstrator," *proc. SPIE* **5382**, p. 595, 2004.
5. A. A. S. Awwal, B. J. Bauman, D. T. Gavel, S. S. Olivier, S. Jones, D. A. Silva, J. L. Hardy, T. B. Barnes, and J. S. Werner, "Characterization and operation of a liquid crystal adaptive optics phoropter," *proc. SPIE* **5169**, p. 104, 2003.
6. L. A. Poyneer and B. A. Macintosh, "Wavefront control for extreme adaptive optics," *proc. SPIE* **5169**, p. 190, 2003.
7. L. A. Poyneer, D. W. Palmer, K. N. LaFortune, and B. Bauman, "Experimental results for correlation-based wavefront sensing," *proc. SPIE* **5894**, p. 207, 2005.
8. S. Thomas, "Optimized centroid computing in a shack-hartmann sensor," *proc. SPIE* **5490**, p. 1238, 2004.
9. L. A. Poyneer, "Advanced techniques for fourier transform wavefront reconstruction," *proc. SPIE* **4839**, p. 1023, 2003.
10. D. T. Gavel *OSA topical meeting on Adaptive Optics Analysis and Methods, June 2005*, 2005.
11. D. T. Gavel, "Tomography for multiconjugate adaptive optics systems using laser guide stars," *proc. SPIE* **5490**, p. 1356, 2004.
12. J. W. Hardy, *Adaptive Optics for Astronomical Telescopes*, Oxford University Press, Inc., New York, NY., 1998.